

Interaction between Ionized and Molecular Gas in the Active Star-Forming Region W31

Kee-Tae Kim and Bon-Chul Koo

Astronomy Program, SEES, Seoul National University, Seoul 151-742, Korea:
kimkt@astro.snu.ac.kr, koo@astrohi.snu.ac.kr

ABSTRACT

We have carried out 21 cm radio continuum, H76 α radio recombination line, and various (^{12}CO , ^{13}CO , CS, & C^{34}S) molecular line observations of the W31 complex. Our radio continuum data show that W31 is composed of two extended HII regions, G10.2–0.3 and G10.3–0.1, each of which comprises an ultracompact HII region, two or more compact components, and diffuse envelope. The W31 cloud appears as an incomplete shell on the whole and consists of southern spherical and northern flat components, which are associated with G10.2–0.3 and G10.3–0.1, respectively. For an assumed distance of 6 kpc, the molecular cloud has a size of 48 pc and a mass of $6.2 \times 10^5 M_\odot$. The IR luminosity-to-mass ratio and the star formation efficiency are derived to be $9 L_\odot/M_\odot$ and 3%, respectively. These estimates are greater than average values of the inner Galactic plane. We detect two large (16 and 11 pc) and massive (2.1×10^5 and $8.2 \times 10^4 M_\odot$) CS-emitting regions in the northern and southern cloud components. The large amount (48% in mass and 16% in area) of dense gas may suggest that the W31 cloud has ability to form rich stellar clusters and that star formation has only recently begun. The extended envelopes of both G10.2–0.3 and G10.3–0.1 are likely to be results of the champagne flows, based on the distributions of ionized and molecular gas and the velocity gradient of H76 α line emission. According to the champagne model, the dynamical ages of the two HII regions would be $(4-12) \times 10^5$ yr. We find strong evidence of bipolar molecular outflows associated with the two ultracompact HII regions. In the vicinity of the ultracompact and compact HII regions in G10.3–0.1, the ^{12}CO $J=2-1/J=1-0$ intensity ratio is high (1.4) and a small but prominent molecular gas hollow exists. Together these observations strongly indicate that the HII regions and their ionizing stars are interacting with the molecular cloud. Therefore, it is most likely that recently formed massive stars are actively disrupting their parental molecular cloud in the W31 complex.

Subject headings: HII regions—ISM: clouds—ISM: individual (W31)—ISM: molecules—radio continuum: ISM — radio lines: ISM—stars: formation

1. Introduction

Stars form in the dense cores of molecular clouds and eventually emerge as visible objects. Thus the molecular gas and dust surrounding newly formed stars should be disrupted. Massive stars are expected to play an important role in dispersing the ambient materials, since they emit strong radiation, stellar winds, and outflows even at their earliest evolutionary stage. Moreover, massive stars could dramatically impact on the surrounding environments through HII regions and supernova explosions. However, direct observational evidence of this conjecture is rarely seen.

W31 is one of the brightest HII region/molecular cloud complex in the inner Galaxy. Kalberla, Goss, & Wilson (1982) suggested on the basis of their sensitive HI absorption line observations that W31 is associated with the expanding 3-kpc arm with a peculiar velocity of $\sim 30 \text{ km s}^{-1}$ and so lies about 6 kpc from the Sun (see also Wilson 1974). We adopt this distance throughout the present paper, although there are some reports that propose different distances, e.g., $14.5 \pm 1.4 \text{ kpc}$ (Corbel et al. 1997) and $3.4 \pm 0.3 \text{ kpc}$ (Blum, Damineli, & Conti 2001). W31 appears as two prominent extended HII regions, G10.2–0.3 and G10.3–0.1, in the radio continuum maps with low ($>1'$) angular resolutions (e.g., Reich, Reich, & Fürst 1990). High-resolution ($<10''$) radio continuum observations show that the central regions of both HII regions form elongated ionization ridges (Woodward, Helfer, & Pipher 1984; Ghosh et al. 1989). Two ultracompact (UC) HII regions, G10.15–0.34 and G10.30–0.15, were found to be located at the peaks of the ionization ridges, respectively (Wood & Churchwell 1989; Kim & Koo 2001). Several other massive young stellar objects were also identified in G10.2–0.3 by near-infrared observations (Blum et al. 2001). These suggest that massive star formation is actively ongoing in the W31 complex. On the other hand, a Crab-like supernova remnant (SNR) G10.0–0.3 is $\sim 10'$ southwest of G10.15–0.34. The SNR is likely to be associated with a soft γ -ray repeater, SGR 1806–20 (Kulkarni et al. 1994). Accordingly, the W31 complex seems to be one of the best laboratories for studying the formation of massive stars and the interaction of massive stars with their parental molecular cloud.

In this paper, we present radio continuum, radio recombination line (RRL), and various molecular line observations of the W31 complex. Our observations aim to investigate the physical characteristics of molecular clouds that are actively forming massive stars, and to explore how massive stars and their natal molecular clouds interact with each other. The observations are described in § 2 and the results are presented in § 3. In § 4 we discuss the physical properties of the W31 molecular cloud and the interaction between ionized and molecular gas in the region. Our main results are summarized in the last section.

2. Observations

2.1. Radio Continuum and Recombination Lines

The radio continuum and RRL data are extracted from the survey of 16 UC HII regions with extended envelopes. The observational details were presented by Kim & Koo (2001). In summary, radio continuum observations were made at 21 cm with the VLA of the NRAO¹ in 1995 February. The array was in the DnC hybrid configuration and the observations were sensitive to structures up to 15'. The final map resulted from two separate pointings of the array. The phase centers were set at G10.15–0.34 and G10.30–0.15, i.e., $(\alpha, \delta)_{1950} = (18^{\text{h}}06^{\text{m}}22\text{s}.5, -20^{\circ}20'05'')$ and $(18^{\text{h}}05^{\text{m}}57\text{s}.9, -20^{\circ}06'26'')$ or $(\alpha, \delta)_{2000} = (18^{\text{h}}09^{\text{m}}21\text{s}.0, -20^{\circ}19'31'')$ and $(18^{\text{h}}08^{\text{m}}56\text{s}.1, -20^{\circ}05'53'')$. The data were calibrated, imaged, and mosaicked using the AIPS. The resulting synthesized half-power beamwidth was $37'' \times 25''$ and the rms noise level of final image was $1.7 \text{ mJy beam}^{-1}$.

H76 α (14.68999 GHz) RRL observations were conducted using the 140 foot telescope of the NRAO in 1997 February and June. The telescope has a FWHM of about 2' and a main beam efficiency of 0.58 at the observing frequency. Both circular polarizations were observed simultaneously using two 1024 channel autocorrelators with 40 MHz bandwidth each, yielding a velocity resolution of 1.59 km s^{-1} after Hanning smoothing.

2.2. Molecular Lines

We have carried out ^{12}CO , ^{13}CO , CS, and C^{34}S line observations of the W31 complex. A summary of the observations is given in Table 1. ^{13}CO J=1–0 and ^{12}CO J=2–1 line observations were made with the 12 m telescope of the NRAO at Kitt Peak using the on-the-fly mapping technique. We used 256 channel filterbanks with 64 MHz and 128 MHz bandwidths as the backend, respectively. A squared area of $30' \times 40'$ centered at $(\alpha, \delta)_{1950} = (18^{\text{h}}06^{\text{m}}09\text{s}.1, -20^{\circ}09'23'')$ was mapped at $20''$ spacing in the ^{13}CO J=1–0 line, while a $5' \times 5'$ region centered at G10.30–0.15 was mapped at $10''$ sampling in the ^{12}CO J=2–1 line. We used positions with some emission as reference positions, $(l, b) = (10^{\circ}15, -1^{\circ}50)$ and $(10^{\circ}05, +0^{\circ}03)$, because we could not find any positions devoid of ^{12}CO and/or ^{13}CO emission near the source. We obtained a sensitive spectrum of each reference position and then added it to the position-switched spectra. The system temperatures were typically 300 K at 110 GHz and 400 K at 230 GHz. We have converted the observed temperatures (T_{R}^*) to the main-beam brightness temperature (T_{b}) using the corrected main-beam efficiencies (η_{mb}^*) provided by the NRAO.

CS J=2–1 line observations were undertaken using the 14 m telescope of the Taeduk Radio Astronomy Observatory (TRAO). We mapped two regions of $11' \times 14'$ and $12' \times 10'$, respectively, centered at G10.15–0.34 and G10.30–0.15 in full-beam ($60''$) spacing. The two UC HII regions were observed in the CS J=3–2 and C^{34}S J=2–1 and J=3–2 lines as well. We used SIS mixer

¹ The National Radio Astronomy Observatory is operated by Associated Universities, Inc., under cooperative agreement with the National Science Foundation

receivers with 256 channel filterbanks of 64 MHz bandwidth. The spectra were obtained by position switching to $(l, b) = (10^\circ 15, 0^\circ 50)$, which was checked to be free from appreciable ($T_A^* < 0.1$ K) CS emission. The system temperature varied in the range 300–500 K at 98 GHz and 600–800 K at 147 GHz. We also made ^{12}CO $J=1-0$ line observations of the region mapped in ^{12}CO $J=2-1$ line emission using a 256 channel filterbank with 256 MHz bandwidth. The system temperature was about 1000 K. The line intensity was obtained on the T_A^* scale from the chopper-wheel calibration.

3. Results

3.1. Radio Continuum and Recombination Line Results

Figure 1 is our 21 cm radio continuum image of the W31 complex. There are two distinct extended HII regions, G10.2–0.3 and G10.3–0.1, in the field. G10.2–0.3 has several compact components, almost all of which are embedded in low-level extended envelope of $10'9 \times 6'7$ (or $19.0 \text{ pc} \times 11.1 \text{ pc}$). The central region is elongated in the east-west direction on the whole and is composed of two strong compact components. The UC HII region G10.15–0.34 lies at the peak of the western one. High-resolution ($\sim 5''$) VLA continuum observations at 5 GHz suggest that the central region comprises about 20 dense ionized clumps (Woodward et al. 1984). The surface brightness declines sharply to the west, while it decreases slowly to the east. Figure 2 shows H76 α spectra observed along $\delta(1950) \simeq -20^\circ 20' 05''$. The center velocity decreases with increasing right ascension. The velocity difference is about 10 km s^{-1} between the central region and the eastern protuberance.

In G10.3–0.1, there are one isolated compact component and two strong ones surrounded by diffuse emission extending over $12'8 \times 4'6$ (or $22.3 \text{ pc} \times 8.0 \text{ pc}$). The two central compact components form an ionization ridge elongated in the northeast-southwest direction. The UC HII region G10.30–0.15 is located at the peak of the western one. The diffuse envelope extends straight in the northwest-southeast direction, which is perpendicular to the central ridge. There is no significant velocity difference between the central region and the envelope. According to Kim & Koo (2001), the UC HII regions and their associated compact components are likely to be excited by the same ionizing sources in both G10.2–0.3 and G10.3–0.1, while the individual compact components may be ionized by separate sources.

3.2. ^{13}CO $J=1-0$ Line Results

Figure 3 exhibits ^{13}CO $J=1-0$ line profiles observed towards G10.15–0.34 and G10.30–0.15. There are three or more velocity components in the lines of sight. In each spectrum, the strongest component is associated with the UC HII region. The center velocities of ^{13}CO gas are shifted by $5-8 \text{ km s}^{-1}$ from those of the ionized gas, marked by the vertical dotted lines. There seem

to be high-velocity wings in the ^{13}CO lines of both UC HII regions, even though the features are significantly confused by multiple velocity components. Shepherd & Churchwell (1996) have also found high-velocity wings in the ^{12}CO $J=1-0$ line of G10.30–0.15, but could not identify them in G10.15–0.34 due to a complex blend of lines. We will discuss in more detail the high-velocity gas using our CS spectra in the next section.

Figure 4 is ^{13}CO line integrated intensity map, obtained by integrating over the velocity range between $v_{\text{LSR}} = 0$ and 22 km s^{-1} . Large crosses indicate the positions of UC HII regions, while small crosses represent the peak positions of the strong compact components without UC HII regions (see Fig. 1). The molecular cloud is very clumpy. There is a large hollow over the central region, which makes the cloud appear as an incomplete shell being open to the northeast. A possible explanation for this morphology is that the cloud has been produced by energetic events near the center, such as strong stellar winds and/or supernova explosions of massive stars, although we have not found any massive star or nonthermal radio continuum emission in the hollow region. As will be discussed in § 4.2, the dynamical age of G10.2–0.3 is similar to that of G10.3–0.1, suggesting that star formation has begun almost simultaneously at the southern spherical and northern flat components. This may be in favor of the above interpretation. It seems that the northern component has been substantially dispersed by massive stars, since a small but conspicuous hollow exists near the UC and compact HII regions, $(\alpha, \delta)_{1950} \approx (18^{\text{h}}05^{\text{m}}58^{\text{s}}, -20^{\circ}05'45'')$ (see § 4.2). In the southern component, on the contrary, the dense ^{13}CO cores associated with the UC and compact HII regions are still strong. It is worthwhile to note that the integrated intensity drops steeply on the eastern boundary of the southern component, in contrast to the radio continuum intensity distribution.

Figure 5 displays the channel maps of the molecular cloud. ^{13}CO emission appears mainly in the velocity range between 2 and 20 km s^{-1} . The channel maps show that the northern and southern components are certainly associated, and reveal more clearly incomplete shell-like morphology of the cloud. The molecular gas shell remains nearly constant in size as the velocity varies, suggesting that it does not dynamically expand or contract. There are small velocity variations in both northern and southern components. As the velocity decreases, strong ^{13}CO emission moves from the western part to the eastern part in the northern component, while it moves from the northeastern part through the northern part to the southern part in the southern component. The ^{13}CO core associated with G10.15–0.34 ($\sim 8 \text{ km s}^{-1}$) is slightly blueshifted from the main shell-like structure ($\sim 12 \text{ km s}^{-1}$). The northern flat component seems to be nearly broken through at the position of the distinctive hollow, which persists over a velocity interval of 10 – 15 km s^{-1} .

Assuming that the molecular gas is in local thermodynamical equilibrium (LTE), ^{13}CO column density, $N(^{13}\text{CO})$, can be computed from the formula (see, e.g., Dickman 1978)

$$N(^{13}\text{CO}) = 2.42 \times 10^{14} \frac{T_{\text{ex}} \int \tau dv}{1 - \exp(-5.29/T_{\text{ex}})} \quad (\text{cm}^{-2}), \quad (1)$$

where T_{ex} is the excitation temperature in K, τ is the optical depth, v is the velocity in km s^{-1} . The

mass of molecular cloud, M_{LTE} , is measured to be $6.20 \times 10^5 M_{\odot}$, provided that ^{13}CO abundance relative to H_2 is 2×10^{-6} (Dickman 1978). In this calculation we assumed that the cloud boundary is $\int T_R^* dv \simeq 10 \text{ K km s}^{-1}$ and that T_{ex} is 30 K in the central regions of the northern and southern components and 15 K in the outer regions, based on our ^{12}CO line data and the Massachusetts-Stony Brook ^{12}CO Galactic Plane Survey (Sanders et al. 1986). Our mass estimate adopted a mean molecular weight of 2.3 to account for the contribution of helium. Table 2 summarizes the physical parameters of the W31 molecular cloud.

3.3. CS Line results

Figure 6 exhibits our CS and C^{34}S line profiles obtained towards G10.15–0.34 and G10.30–0.15. The line parameters of these spectra are presented in Table 3. There is a single velocity component along the line of sight and it is associated with each UC HII region. The center velocity of CS gas is in good agreement with that of ^{13}CO gas. The CS $J=2-1$ and $J=3-2$ lines of both UC HII regions show distinct high-velocity wings. This implies that dense gas exists in high-velocity molecular components. There are a few tens of massive star-forming regions where high-velocity wings have been observed in the CS lines. For example, Plume, Jaffe, & Evans (1992) detected CS $J=7-6$ line emission in 104 massive star-forming regions, selected originally by the presence of an H_2O maser, and found high-velocity wings in more than 18 out of them. The full widths of the CS $J=2-1$ lines are about 50 km s^{-1} at typical rms noise level for G10.15–0.34 and about 30 km s^{-1} for G10.30–0.15. These values are similar to those expected from the ^{13}CO lines, respectively. The CS $J=3-2$ line of G10.30–0.15 has very similar shape and full width as the CS $J=2-1$ line, while the CS $J=3-2$ line of G10.15–0.34 has a different asymmetric shape and a smaller (20 km s^{-1}) full width than the CS $J=2-1$ line. The full width of the CS $J=2-1$ line of G10.15–0.34 is comparable to that of G5.89–0.39, which drives one of the most energetic outflows in the Galaxy (Harvey & Forveille 1988). On the other hand, we can not find high-velocity wings in the CS lines observed in the surrounding regions of both UC HII regions. It seems mainly because the extents of CS outflows are $\lesssim 1'$, taking into account that CO outflows observed in massive star-forming regions usually have linear sizes of $\lesssim 2 \text{ pc}$ (Ridge & Moore 2001; Beuther et al. 2002). So high-resolution CS line observations are required to confirm whether the high-velocity gas is indeed due to bipolar molecular outflows, and to explore the physical and dynamical properties of the outflows.

Assuming that the excitation temperature and the beam filling factor are identical in the CS and C^{34}S lines in each transition, we determine the optical depth of C^{34}S line emission, τ_p , from the peak brightness temperature ratio using the following formula

$$T_b(\text{C}^{34}\text{S})/T_b(\text{CS}) = [1 - \exp(-\tau_p)]/[1 - \exp(-\tau_p R)]. \quad (2)$$

The estimated values are listed in Table 3. Here the CS to C^{34}S abundance ratio, R , was assumed to be equal to the terrestrial value (22.5).

Figure 7 shows integrated CS J=2–1 line intensity maps. The CS gas distribution agrees well with the ^{13}CO gas distribution in the dense regions of the northern and southern components. We can see the prominent hollow near G10.30–0.15 in the CS gas distribution as well. The UC HII regions correspond to the peaks of CS cores, while the compact components without UC HII regions do not. This seems to be consistent with the result of Kim & Koo (2001) that the compact components with UC HII regions are smaller and denser than those without UC HII regions. Based on the observation they suggested that the former are in an earlier evolutionary stage than the latter. We have also found the same trend in several other UC HII regions with extended envelopes that have two or more compact components. The results will be presented in a separate paper (Kim & Koo 2002).

If CS line emission originates from regions in LTE and is optically thin, the CS column density, $N(\text{CS})$, is given as

$$N(\text{CS}) = 1.88 \times 10^{11} T_r \exp(7.05/T_r) \int T_b dv \quad (\text{cm}^{-2}), \quad (3)$$

where T_r is the rotation temperature in K, T_b is the brightness temperature in K, and v is the velocity in km s^{-1} . If we take a fractional CS abundance to H_2 of 1×10^{-9} (Linke & Goldsmith 1980; Frerking et al. 1980), the total masses of CS-emitting regions are $2.13 \times 10^5 M_\odot$ for G10.2–0.3 and $0.82 \times 10^5 M_\odot$ for G10.3–0.1. In these calculations T_r was assumed to be 30 K on the basis of the results of studies on dense cores in massive star-forming regions (e.g., Snell et al. 1984; Linke & Goldsmith 1980). Table 2 lists the physical parameters of the CS-emitting regions.

3.4. ^{12}CO J=1–0 and J=2–1 Line Results

We obtained ^{12}CO J=2–1/J=1–0 integrated intensity ratio map for the squared area of $\sim 5' \times 5'$ centered at G10.30–0.15, after convolving ^{12}CO J=2–1 data to the resolution ($53''$) of ^{12}CO J=1–0 data. The integrated velocity range was $v_{\text{LSR}} = 0\text{--}22 \text{ km s}^{-1}$. Figure 8 shows the distribution of ^{12}CO J=2–1/J=1–0 ratio (grey scale) overlaid with the distribution of ^{12}CO J=2–1 line integral (contours). The ratio peaks over the dense cores associated with the UC and compact HII regions and is low ($\lesssim 1.2$) over the hollow region. The estimated values are between 1.0 and 2.0. The average value is 1.4, which is much greater than typical value (0.5–0.8) for molecular clouds in the Galactic disk (e.g., Sakamoto et al. 1997). Such a high (> 1.0) ratio is observed towards the areas around HII regions in molecular clouds undergoing massive star formation, e.g., Orion A molecular cloud (Castets et al. 1990; Sakamoto et al. 1994), Sgr A molecular cloud (Oka et al. 1996), and W51B molecular cloud (Koo 1999).

If a molecular cloud has a uniform temperature, these high ratios can be obtained when the molecular gas is warm, dense, and less opaque. For example, Sakamoto et al. (1994) showed on the basis of an one-zone large velocity gradient (LVG) analysis that ratios greater than unity are

produced when the CO-emitting regions have $T_{\text{ex}} \gtrsim 40$ K, $n(\text{H}_2) \gtrsim 1 \times 10^3 \text{ cm}^{-3}$, and $\tau_{21} < 5$. In this model the ratio variation is mainly attributed to the density variation of unresolved clumps that constitute the cloud. However such a single-temperature model does not seem to be applicable to our case, since the ratio of ^{12}CO $J=1-0$ and ^{13}CO $J=1-0$ line intensities, $^{12/13}R_{1-0}$, ranges between 1.3 and 6.7 with an average of 2.7, indicating that ^{12}CO line emission is optically thick ($\tau_{21} \gg 5$). On the other hand, the high ratios can also be obtained when a dense molecular cloud is externally heated by strong far-ultraviolet (FUV) radiation. Gierens, Stutzki, & Winnewisser (1992) performed a detailed ^{12}CO and ^{13}CO line radiative transfer analysis for spherically symmetric clumps irradiated by intense FUV radiation, and showed that the ratios > 1 observed in the Orion A molecular cloud are easily explained by the temperature and abundance variations within the photodissociation region layer of the clumps. If we adopt their results, we can derive $\langle n(\text{H}_2) \rangle$ and $\langle N(\text{H}_2) \rangle / \Delta v$ of the CO-emitting regions from the ratio of ^{12}CO $J=2-1$ and $J=1-0$ line intensities, $^{12}R_{2-1/1-0}$, and $^{12/13}R_{1-0}$ using their Figures 3 and 5. The $^{12}R_{2-1/1-0}$'s are 1.0–2.4 with an average of 1.6. The average values for $^{12/13}R_{1-0}$ and $^{12}R_{2-1/1-0}$ suggest that $\langle N(\text{H}_2) \rangle / \Delta v \gtrsim 1 \times 10^{22} \text{ cm}^{-2} (\text{km s}^{-1})^{-1}$ and $\langle n(\text{H}_2) \rangle \simeq 10^4 \text{ cm}^{-3}$. The $^{12}R_{2-1/1-0}$ is lower ($\lesssim 1.4$) over the hollow region than the surrounding regions, while the $^{12/13}R_{1-0}$ is higher ($\gtrsim 4$). This implies, as expected, that $\langle n(\text{H}_2) \rangle$ and $\langle N(\text{H}_2) \rangle / \Delta v$ are both lower in the hollow region, i.e., $\langle N(\text{H}_2) \rangle / \Delta v = (0.3-1.0) \times 10^{22} \text{ cm}^{-2} (\text{km s}^{-1})^{-1}$ and $\langle n(\text{H}_2) \rangle = (1.5-6.0) \times 10^3 \text{ cm}^{-3}$.

4. Discussion

4.1. Physical Characteristics of the W31 Molecular Cloud

The W31 molecular cloud is classified as a giant molecular cloud (GMC) based on the physical parameters determined from the ^{13}CO line observations. The CS-emitting regions of W31 are much more massive and larger than those ($10^2-10^4 M_{\odot}$ in mass and 0.5–5 pc in size) of molecular clouds associated with Sharpless HII regions, which are excited by single late O or early B stars (Zinchenko et al. 1994; Carpenter, Snell, & Schloerb 1995). Hence the fraction of dense ($> 10^4 \text{ cm}^{-3}$) molecular gas may be much higher in the W31 cloud than in the molecular clouds with Sharpless HII regions. For W31 as a whole, the CS-emitting regions contain 48% of the total mass and occupy 16% of the total area (see Table 2). In comparison, these values are, respectively, one order of magnitude greater than estimates (2% and $< 1\%$) for the Gemini OB1 cloud complex with about 10 Sharpless HII regions, which has a similar total mass to the W31 cloud (Carpenter et al. 1995). This seems to be consistent with the observation that more luminous *IRAS* sources tend to be associated with more massive CS cores in the Gemini complex, suggesting that more massive cores in general form more massive stars (Carpenter et al. 1995). Similar results have been found in the Orion B (L1630) molecular cloud (Lada 1992) and the Rosette molecular cloud (Phelps & Lada 1997). In these molecular clouds the embedded clusters are associated with the most massive dense cores. These observations indicate that both high gas density and high gas mass are required for the formation of stellar clusters. On the other hand, the CS-emitting regions of W31 are further

more massive and larger than those of some other GMCs undergoing active massive star formation, such as M17 (Snell et al. 1984) and Orion B (Lada et al. 1991). This difference is likely due to difference in evolution (destruction of dense cores by massive stars) as well as difference in the initial physical properties, since some newly formed massive stars have already emerged as visible objects in the regions (e.g., Stephenson & Hobbs 1961; Warren & Hesser 1978).

The ratio of infrared (IR) luminosity to mass is a good measure of the massive star formation activity of molecular clouds. The ratio varies widely from cloud to cloud, and shows little correlation with cloud mass from 10^2 to $10^7 M_\odot$ or location in the Galaxy (Mooney & Solomon 1988; Scoville & Good 1989; Carpenter, Snell, & Schloerb 1990). We estimate the ratio for the W31 molecular cloud using *IRAS* HIgh REsolution processing (HIRES) images at $60 \mu\text{m}$ and $100 \mu\text{m}$. After a smooth background emission is removed from each image, the total flux densities at $60 \mu\text{m}$ and $100 \mu\text{m}$, F_{60} and F_{100} , are measured to be $(7.4 \pm 0.8) \times 10^4 \text{ Jy}$ and $(1.09 \pm 0.10) \times 10^5 \text{ Jy}$ within the could boundary, respectively. Here we took average intensities on the cloud boundary as the background emission levels. The total IR luminosity in the wavelength range $1\text{--}500 \mu\text{m}$, L_{IR} , can be calculated from F_{60} and F_{100} in Jy using the following formula (Lonsdale et al. 1985; Lee et al. 1996)

$$L_{\text{IR}} = 0.394 R(\overline{T}_d, \beta) [F_{100} + 2.58 F_{60}] d^2 \quad (L_\odot), \quad (4)$$

where T_d is the $60/100 \mu\text{m}$ color temperature in K, β is the index in the emissivity law, $Q_{\text{abs}} \sim \lambda^{-\beta}$, and d is the source distance in kpc. The $R(\overline{T}_d, \beta)$ is color correction factor that accounts for the flux radiated outside the $60 \mu\text{m}$ and $100 \mu\text{m}$ *IRAS* bands. If β is assumed to be 1 (Hildebrand 1983), L_{IR} is derived to be $5.8 \times 10^6 L_\odot$, which gives $L_{\text{IR}}/M_{\text{LTE}} = 9.4 L_\odot/M_\odot$. This estimate is much greater than the average ratio ($2.8 L_\odot/M_\odot$) of all molecular clouds in the inner Galactic plane, but is comparable to the median value ($7 L_\odot/M_\odot$) for GMCs with HII regions (Scoville & Good 1989).

We also derive star formation efficiency, $\text{SFE} \equiv M_*/(M_* + M_{\text{cloud}})$, of the W31 cloud. The stellar mass M_* was computed from the Lyman continuum photon flux N'_c measured by radio continuum observations of G10.2–0.3 and G10.3–0.1, $2.7 \times 10^{50} \text{ photons s}^{-1}$ (Kim & Koo 2001). Here we adopt $\langle M_* \rangle / \langle N'_c \rangle = 5.7 \times 10^{-47} M_\odot (\text{photons s}^{-1})^{-1}$, which was determined by McKee & Williams (1997) using the initial mass function of Scalo (1986) and the parameters of OB stars of Vacca, Garmann, & Shull (1996). The SFE estimated for the entire cloud is 3%, which is somewhat greater than the Galactic median value of $\sim 2\%$ (Myers et al. 1986). On the other hand, the SFE's for the two CS-emitting regions are derived to be 6% and 4%, respectively (Table 3).

4.2. Interaction between Ionized and Molecular Gas

Figure 9 shows the ionized gas distribution (contours) superposed on the molecular gas distribution (color). For both G10.2–0.3 and G10.3–0.1, the morphology of extended envelope seems

to be largely determined by the distribution of the ambient molecular gas. In G10.2–0.3, the radio continuum surface brightness decreases slowly to the east while it drops rapidly to the west. This surface brightness behavior can be naturally understood if the central part of G10.2–0.3 is situated within the molecular cloud and the eastern protuberance is a result of the champagne flow (Israel 1978; Tenorio-Tagle 1979). A large (>10 km s $^{-1}$) velocity gradient exists between the central and eastern parts (see Fig. 2), which is compatible with what would be expected from the champagne flow model. On the other hand, the extended envelope of G10.3–0.1 has a bipolar morphology. Such a morphology can be created by the champagne flow in case where the HII region forms in a flat molecular cloud (Bodenheimer, Tenorio-Tagle, & Yorke 1979; Tenorio-Tagle, Yorke, Bodenheimer 1979). Indeed the distribution of molecular gas in the region is severely elongated in the direction orthogonal to the bipolar axis of G10.3–0.1 (see also Fig. 7b). Therefore, the extended envelope of G10.3–0.1 is also likely to be a consequence of the champagne flow. However, we have not observed any significant velocity difference between the central region and the envelope. This might be due to a small inclination. The velocity of a champagne flow is determined by the pressure contrast at the cloud boundary and can increase up to about 30 km s $^{-1}$ (Tenorio-Tagle 1979). Since the farthest boundary is ~ 12 pc (7') from the central region for both G10.2–0.3 and G10.3–0.1, their dynamical ages may be in the range $(4\text{--}12) \times 10^5$ yr. For G10.2–0.3, our estimate matches with the result of Blum et al. (2001), who derived a mean age of $\sim 1 \times 10^6$ yr for the embedded cluster associated with the eastern compact component in the central region, based on their near-IR photometry and spectroscopy.

A striking feature is the distinctive molecular gas hollow in the northern flat component of the W31 cloud. The hollow is ~ 4 pc (2') in size. It is located close to the UC and compact HII regions. The thickness of the flat molecular cloud is much smaller at the hole position than other parts. These observations strongly suggest that the hollow might have been produced due to the dispersion and destruction of molecular gas by the HII regions and their ionizing stars. This view is supported by the fact that the ^{12}CO $J=2\text{--}1/J=1\text{--}0$ integrated intensity ratio exceed unity around the UC and compact HII regions, implying that the HII regions and their central stars are closely interacting with the surrounding molecular materials. It is well known that the surrounding gas and dust of newly formed massive stars should be eventually dispersed and destroyed by strong radiation, stellar winds, and HII regions.

If the molecular gas column density of the hollow region had been equal to the average value of the surrounding regions, which have $\int T_R^* dv \gtrsim 25$ K km s $^{-1}$, the amount of molecular gas dispersed by the massive stars would be $(4\pm 1) \times 10^3 M_\odot$. The quoted error represents variation in the measured mass depending on the assumed threshold value for the surrounding regions. Our estimate is not very different from the ionized gas mass of G10.3–0.1, $2 \times 10^3 M_\odot$, determined from radio continuum observations (Kim & Koo 2001). The derived mass and dynamical age imply that the disruption rate of the molecular cloud is $(3\text{--}10) \times 10^{-3} M_\odot \text{ yr}^{-1}$, which is very similar to the results of two-dimensional numerical calculations for the champagne flows in various conditions, $(5\text{--}10) \times 10^{-3} M_\odot \text{ yr}^{-1}$ (Yorke, Bodenheimer, & Tenorio-Tagle 1982). Whitworth (1979) also

performed a semi-analytic study on the efficiency with which massive stars destroy their parental molecular clouds and showed that the disruption rate is determined by the Lyman continuum photon flux, the ambient density, and the elapse time. The Lyman continuum photon flux of G10.3–0.1 is 5.5×10^{49} photons s $^{-1}$ (Kim & Koo 2001). The average density of the surrounding regions with $\int T_R^* dv \gtrsim 25$ K km s $^{-1}$ is $\sim 1 \times 10^3$ cm $^{-3}$. In that case the disruption rate is $(5 \pm 1) \times 10^{-3} M_\odot$ yr $^{-1}$. This value is in good agreement with the rate estimated above, too. In addition to strong radiation, the bipolar outflow associated with G10.30–0.15 might have played a role in the dispersion process. Therefore, it is most likely that the northern flat molecular cloud is being disrupted by newly formed massive stars. This may also be true for the southern spherical molecular cloud, although compelling observational evidence for molecular gas disruption have not been found except the champagne flow.

5. Conclusions

We have carried out 21 cm radio continuum, H76 α RRL, ^{12}CO , ^{13}CO , CS, and C^{34}S line observations of the W31 HII region/molecular cloud complex. The physical parameters of the W31 cloud are largely comparable to those of other GMCs that are undergoing active massive star formation. However, the CS-emitting regions are more massive and larger than those of some other GMCs with indicators of massive star formation. The large amount of dense ($> 10^4$ cm $^{-3}$) gas implies that the W31 cloud has ability to form rich stellar clusters and suggests, together with the young dynamical ages ($\lesssim 1 \times 10^6$ yr) of G10.2–0.3 and G10.3–0.1, that star formation has recently begun in the cloud. On the other hand, we have found high-velocity molecular gas towards G10.15–0.34 and G10.30–0.15, which are likely due to bipolar outflows. The extended envelopes of both G10.2–0.3 and G10.3–0.1 may be results of the champagne flows, based on the distributions of ionized and molecular gas and the velocity gradient of RRL emission. In the vicinity of the UC and compact HII regions in G10.3–0.1, a distinctive molecular gas hollow is present and the ^{12}CO $J=2-1/J=1-0$ line intensity ratio exceeds unity. Together these observations support that the HII regions and their ionizing stars are strongly interacting with the surrounding molecular materials. Therefore, W31 is a good example showing not only formation of massive stars but also destruction of their parental molecular cloud by them.

We are grateful to Bob Blum, John Carpenter, Youngung Lee, and Young Chol Minh for helpful comments, and Yong-Sun Park for giving us part of his observing time at the TRAO. We also thank the staff at the IPAC in Caltech for processing the *IRAS* HIRES maps for W31 region. This work has been supported by a bilateral KOSEF-Korea and CONACyT-México agreement (2000-113-01-2), and also BK21 Program, Ministry of Education, Korea through SEES.

REFERENCES

Beuther, H., Schilke, P., Sridharan, T. K., Menten, K. M., Walmsley, C. M., & Wyrowski, F. 2002, *A&A*, 383, 892

Blum, R. D., Damineli, A., & Conti, P. S. 2001, *AJ*, 121, 3149

Bodenheimer, P., Tenorio-Tagle, G., & Yorke, H. W. 1979, *ApJ*, 233, 85

Carpenter, J. M., Snell, R. L., & Schloerb, F. P. 1990, *ApJ*, 362, 147
———. 1995, *ApJ*, 450, 201

Castets, A., Duvert, G., Dutrey, A., Bally, J., Langer, W. D., & Wilson, R. W. 1990, *A&A*, 234, 469

Corbel, S., Wallyn, P., Dame, T. M., Durouchoux, P., Mahoney, W. A., Vilhu, O., & Grindlay, J. E. 1997, *ApJ*, 478, 624

Dickman, R. L. 1978, *ApJS*, 37, 407

Frerking, M. A., Wilson, R. W., Linke, R. A., & Wannier, P. G. 1980, *ApJ*, 240, 65

Gierens, K. M., Stutzki, J., & Winnewisser, G. 1992, *A&A*, 259, 271

Ghosh, S. K., Iyengar, K. V. K., Rengarajan, T. N., Tandon, S. N., Verma, R. P., & Daniel, R. R. 1989, *ApJ*, 347, 338

Harvey, P. M., & Forveille, T. 1988, *A&A*, 197, L19

Hildebrand, R. H. 1983, *QJRAS*, 24, 267

Israel, F. P. 1978, *A&A*, 70, 769

Kalberla, P. M. W., Goss, W. M., & Wilson, T. L. 1982, *A&A* 106, 167

Kim, K.-T., & Koo, B.-C. 2001, *ApJ*, 549, 979

Kim, K.-T., & Koo, B.-C. 2002, in preparation

Koo, B.-C. 1999, *ApJ*, 518, 760

Kulkarni, S. R., Frail, D. A., Kassim, N. E., Murakami, T., & Vasisht, G. 1994, *Nature*, 368, 129

Lada, E. A. 1992, *ApJ*, 393, L25

Lada, E. A., Bally, J., & Stark, A. A. 1991, *ApJ*, 368, 432

Lee, Y., Snell, R. L., & Dickman, R. L. 1996, *ApJ*, 472, 275

Linke, R. A., & Goldsmith, P. F. 1980, *ApJ*, 235, 437

Lonsdale, C. J., Helou, G., Good, J. C., & Rice, W. L. 1985, Catalogued Galaxies and Quasars Observed in the *IRAS* Survey (Washington, DC: GPO)

McKee, C. F., & Williams, J. P. 1997, *ApJ*, 476, 144

Mooney, T. J., & Solomon, P. M. 1988, *ApJ*, 334, L51

Myers, P. C., Dame, T. M., Thaddeus, P., Cohen, R. S., Silverberg, R. F., Dwek, E., & Hauser, M. G. 1986, *ApJ*, 301, 398

Oka, T., Hasegawa, T., Handa, T., Hayashi, M., & Sakamoto, S. 1996, *ApJ*, 460, 334

Phelps, R. L., & Lada, E. A. 1997, *ApJ*, 477, 176

Plume, R., Jaffe, D. T., & Evans, N. J., II 1992, *ApJS*, 78, 505

Reich, W., Reich, P., & Fürst, E. 1990, *A&AS*, 83, 539

Ridge, N. A., & Moore, T. J. T. 2001, *A&A*, 378, 495

Sakamoto, S., Hayashi, M., Hasegawa, T., Handa, T., & Oka, T. 1994, *ApJ*, 425, 641

Sakamoto, S., Hasegawa, T., Handa, T., Hayashi, M., & Oka, T. 1997, *ApJ*, 486, 276

Sanders, D. B., Clemens, D. B., Scoville, N. Z., & Solomon, P. M. 1986, *ApJS*, 60, 1

Scalo, J. 1986, *Fund. Cosmic Phys.*, 11, 1

Scoville, N. Z., & Good, J. C. 1989, *ApJ*, 339, 149

Shepherd, D. S., & Churchwell, E. 1996, *ApJ*, 457, 267

Snell, R. L., Goldsmith, P. F., Erickson, N. R., Mundy, L. G., & Evans, N. J. II 1984, *ApJ*, 276, 625

Stephenson, C. B., & Hobbs, R. W. 1961, *AJ*, 66, 186

Tenorio-Tagle, G. 1979, *A&A*, 71, 59

Tenorio-Tagle, G., Yorke, H. W., & Bodenheimer, P. 1980, *A&A*, 80, 110

Vacca, W. D., Garmany, C. D., & Shull, J. M. 1996, *ApJ*, 460, 914

Warren, W. H. II, & Hesser, J. E. 1978, *ApJS*, 36, 497

Wilson, T. L. 1974, *A&A*, 31, 83

Wood, D. O., & Churchwell, E. 1989, *ApJS*, 69, 831

Woodward, C. E., Helfer, H. L., & Pipher, J. L. 1984, *MNRAS*, 209, 209

Yorke, H. W., Bodenheimer, P., & Tenorio-Tagle, G. 1982, *A&A*, 108, 25

Zinchenko, I., Forssström, V., Lapinov, A., & Mattila, K. 1994, *A&A*, 288, 601

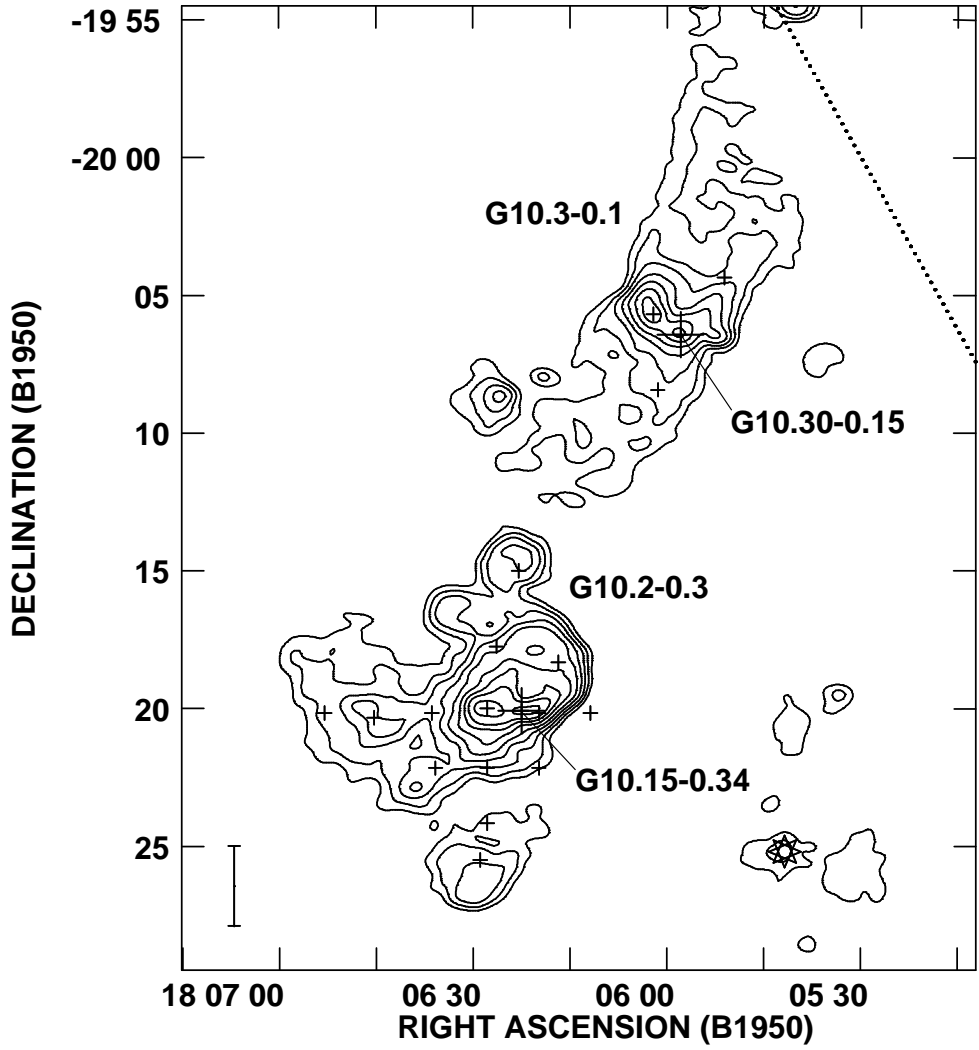


Fig. 1.— 21 cm radio continuum image of W31 made with the VLA (DnC array). This image is corrected for the primary-beam attenuation. The synthesized beam is $37'' \times 25''$ at P.A.=76°. Contours are 10, 30, 70, 150, 300, 600, 1000, 1500, and 2300 mJy beam $^{-1}$. Large crosses are the positions of G10.15–0.34 and G10.30–0.15, while small crosses are the positions where H76 α line emission was observed. The SNR G10.0-0.3 is marked by an eight-pointed star and the Galactic midplane is represented by the dotted line. A 5 pc linear scale bar is shown in the bottom left corner.

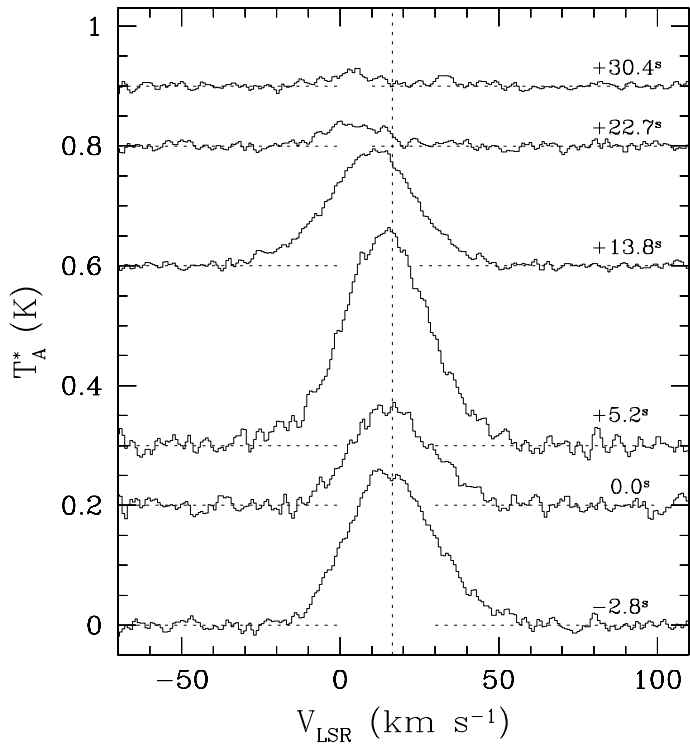


Fig. 2.— H76 α line spectra observed along $\delta(1950) \simeq -20^{\circ}20'05''$ in G10.2–0.3. Right ascension offsets with respect to G10.15–0.34 are given in second on the right side. The vertical dotted line marks the center velocity of H76 α line emission observed toward G10.15–0.34, $v_{\text{LSR}} = 16.4 \text{ km s}^{-1}$.

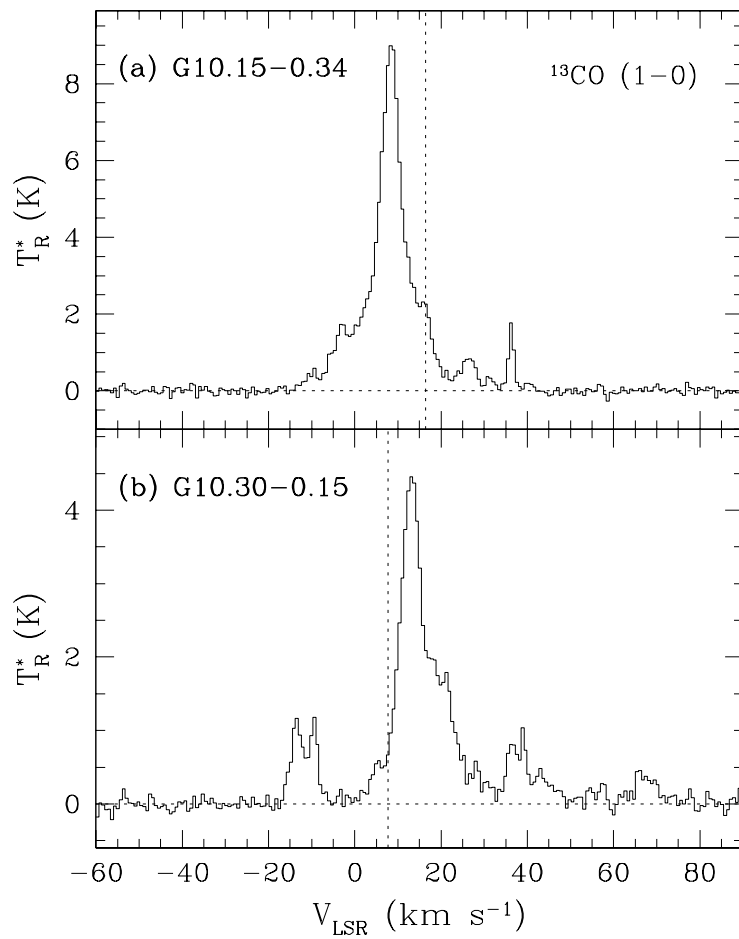


Fig. 3.— ^{13}CO $J=1-0$ line profiles obtained towards (a) G10.15–0.34 and (b) G10.30–0.15. In each panel, the vertical dotted line indicates the center velocity of H76 α line.

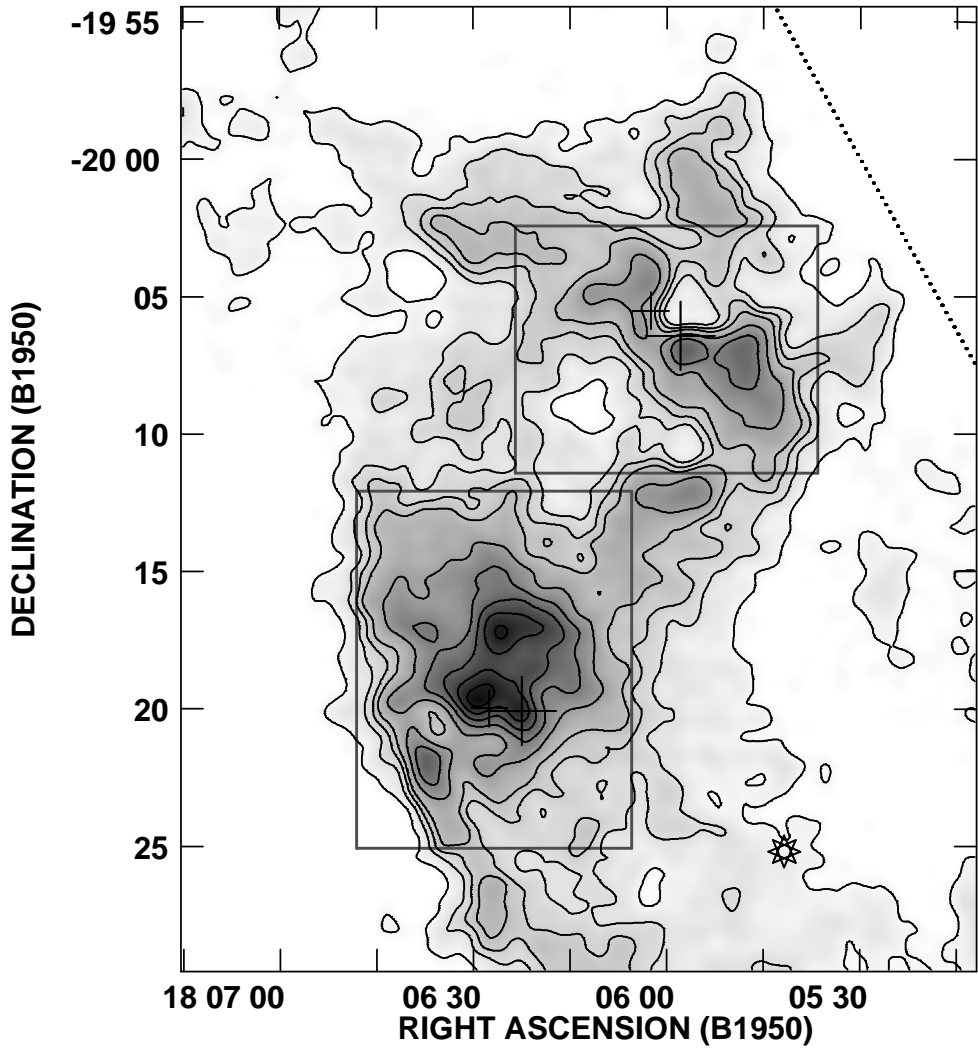


Fig. 4.— ^{13}CO $J=1-0$ integrated intensity map. The integrated velocity range is from $v_{\text{LSR}}=0$ to 22 km s^{-1} . Contour levels are 13, 20, 25, 30, 40, 50, 60, 70 and 80 K km s^{-1} and grey scale flux range is $10-86 \text{ K km s}^{-1}$. The boxes show the areas covered by our CS $J=2-1$ line observations. Large and small crosses represent the UC HII regions and strong compact components without UC HII regions, respectively. The SNR G10.0-0.3 is marked by an eight-pointed star and the Galactic midplane is indicated by the dotted line.

Fig. 5.— Channel maps of ^{13}CO $J=1-0$ line emission. The center velocity is given in km s^{-1} at the upper-right corner in each panel. Contours are 1, 2, 3, 4, 6, and 8 K and grey scale flux range is 0.5–10.0 K. Symbols are the same as in Figure 4.

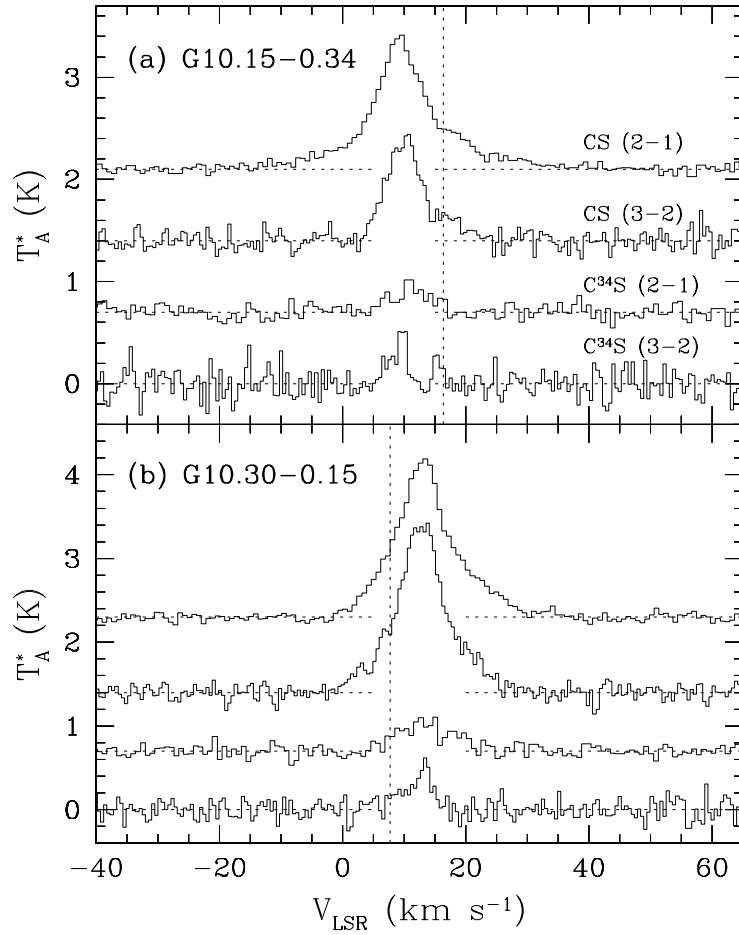


Fig. 6.— CS $J=2-1$ and $J=3-2$ and C^{34}S $J=2-1$ and $J=3-2$ line profiles observed towards (a) G10.15–0.34 and (b) G10.30–0.15. The center velocity of $\text{H76}\alpha$ line is marked by the vertical dotted line in each panel.

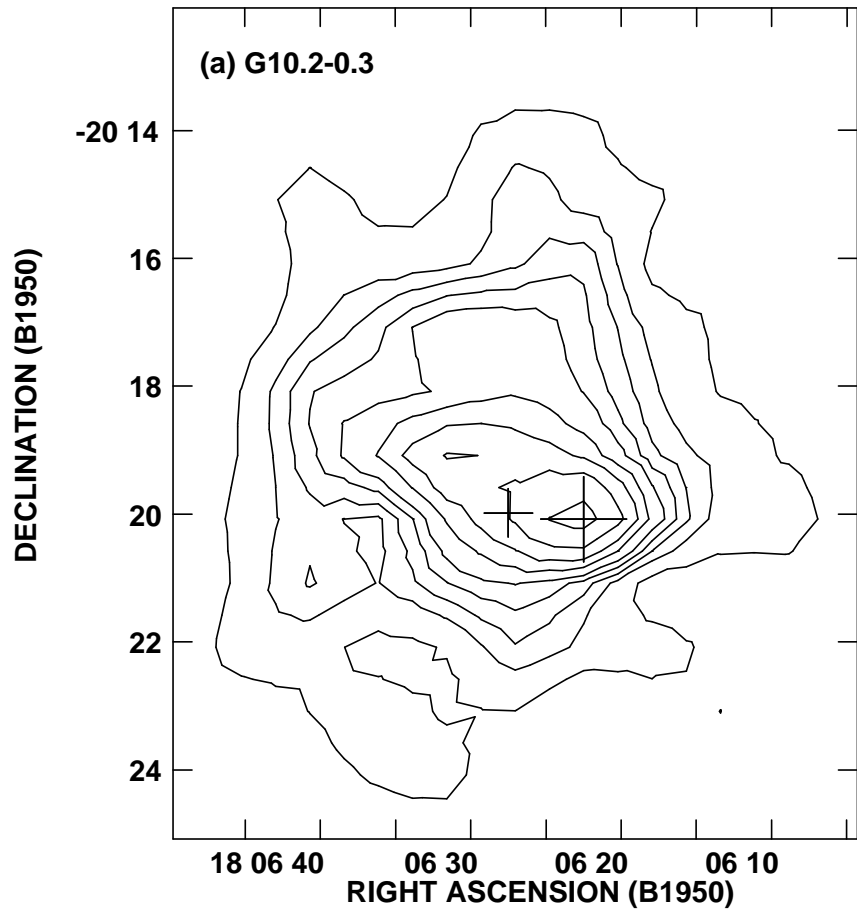
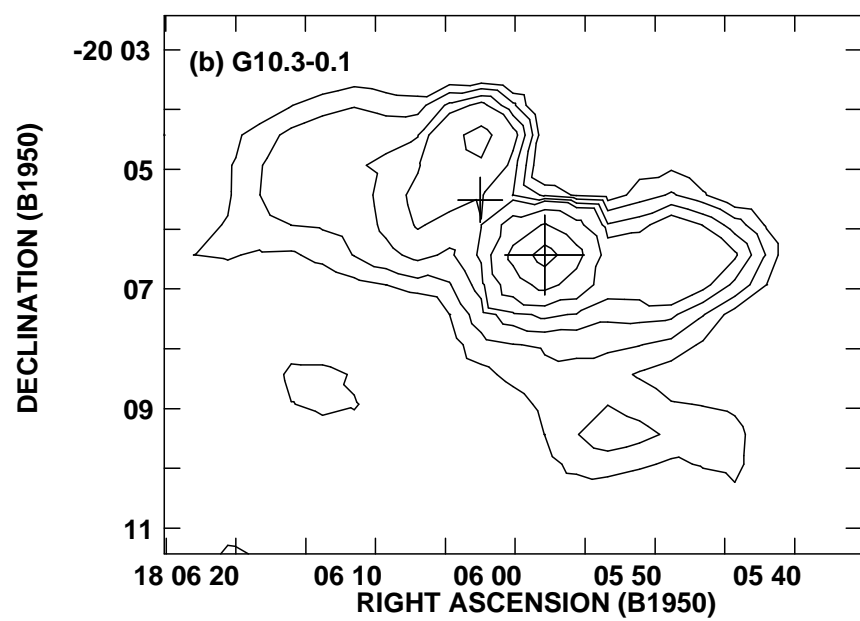


Fig. 7.— CS J=2–1 integrated intensity maps of (a) G10.2–0.3 and (b) G10.3–0.1. Contour levels are 1.5, 3, 4, 5, 6, 7.5, 9, 11, and 14 K km s⁻¹ in (a), and 1.2, 2, 3, 4, 7, 12, and 18 K km s⁻¹ in (b). Large and small crosses represent the UC HII regions and strong compact components without UC HII regions, respectively.



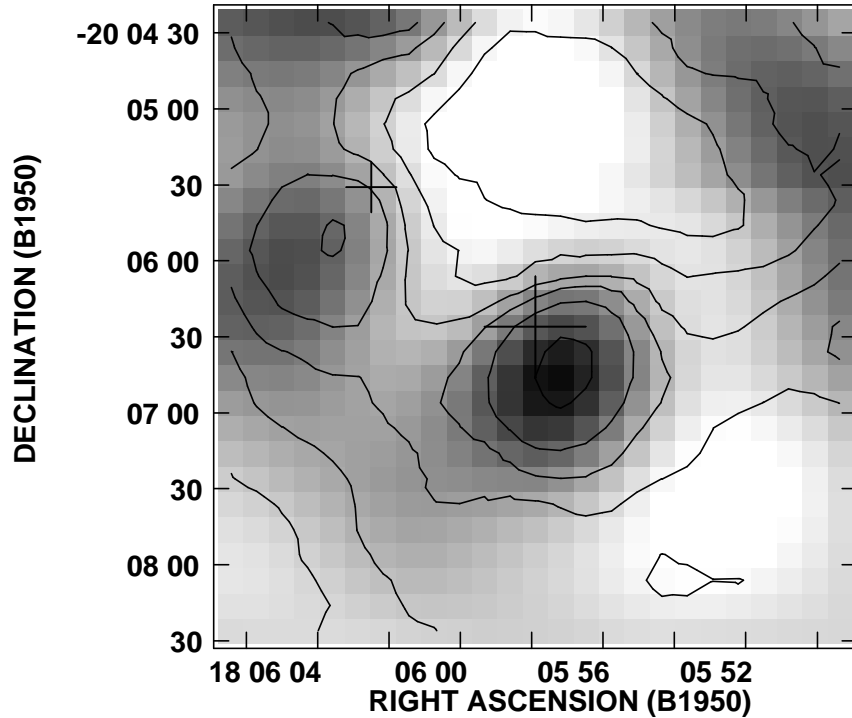


Fig. 8.— ^{12}CO $J=2-1/J=1-0$ integrated intensity ratio map (grey scale) and ^{12}CO $J=2-1$ integrated intensity map (contours) of a $\sim 5' \times 5'$ area around G10.30–0.15. Grey scale flux range is 1.2–2.0 and contours are 80, 100, 120, 140, 170, and 240 K km s^{-1} . Large cross represents G10.30–0.15, while small cross indicates the strong compact components without UC HII region.

Fig. 9.— ^{13}CO integrated intensity map (color) and 21 cm radio continuum image (contours). The integrated velocity range is 0–22 km s^{-1} . Contour levels are 10, 30, 70, 200, 500, 1000, and 2200 mJy beam $^{-1}$. The color wedge on the right shows the integrated intensity range. Crosses represent the positions of G10.15–0.30 (*upper*) and G10.34–0.15 (*lower*).

Table 1. MOLECULAR LINES OBSERVED

Telescope and Transition	Frequency (GHz)	Resolution		FWHM ($''$)	η_{mb}	OFF (l, b)	Observation Date
		Δf (kHz)	Δv (km s $^{-1}$)				
NRAO 12-m							
^{13}CO J=1–0	110.20135	250	0.68	60	0.84 ^a	(10°15, −1°50) ^b	1997 June
^{12}CO J=2–1	230.58300	500	0.62	27	0.51 ^a	(10.05, +0.30) ^b	2000 March
TRAO 14-m							
CS J=2–1	97.98095	250	0.77	60	0.48	(10.15, +0.50)	1997 March
CS J=3–2	146.96904	250	0.51	46	0.39	(10.15, +0.50)	2000 March
C^{34}S J=2–1	96.41298	250	0.77	60	0.48	(10.15, +0.50)	2000 March
C^{34}S J=3–2	144.61711	250	0.51	46	0.39	(10.15, +0.50)	2000 March
^{12}CO J=1–0	115.27120	1000	2.60	53	0.46	(10.05, +0.30) ^b	2000 March

^aCorrected main beam efficiency η_{mb}^* , $T_{\text{b}}=T_{\text{R}}^*/\eta_{\text{mb}}^*$.

^bReference positions with some ^{12}CO and/or ^{13}CO emission.

Table 2. ^{13}CO J=1–0 AND CS J=2–1 LINE OBSERVATIONAL RESULTS

Transition	Source	R (pc)	M_{LTE} ($10^4 M_{\odot}$)	$n(\text{H}_2)$ (10^2 cm^{-3})	Δv^{a} (km s^{-1})	$\log N'_c^{\text{b}}$ (s^{-1})	M_{*} ($10^4 M_{\odot}$)	SFE (%)
^{13}CO J=1–0	W31	24.1	62.0	2.0	8.2	50.43	1.54	3
CS J=2–1	G10.2–0.3	8.0	21.3	19.2	10.0	50.33	1.22	6
	G10.3–0.1	5.6	8.2	21.7	5.4	49.74	0.31	4

^aFWHM of the average spectrum of the entire mapping area.

^bTaken from Kim & Koo 2001.

Table 3. CS AND C³⁴S LINE PARAMETERS

Source and Transition	v_{LSR} (km s ⁻¹)	T_{A}^* (K)	Δv (km s ⁻¹)	τ_{p}
G10.15–0.34				
CS J=2–1	9.6	1.31	8.8	...
CS J=3–2	10.8	1.05	7.1	...
C ³⁴ S J=2–1	10.4	0.32	3.1	0.28
C ³⁴ S J=3–2	10.3	0.50	2.6	0.65
G10.30–0.15				
CS J=2–1	13.5	1.90	8.8	...
CS J=3–2	13.8	2.00	7.7	...
C ³⁴ S J=2–1	15.1	0.40	7.0	0.24
C ³⁴ S J=3–2	13.4	0.62	2.1	0.37

This figure "f5.jpg" is available in "jpg" format from:

<http://arXiv.org/ps/astro-ph/0204309v1>

This figure "f9.jpg" is available in "jpg" format from:

<http://arXiv.org/ps/astro-ph/0204309v1>